Supplementary Information

Layer Separated V_2O_5-PEG-Amine Hybrid Cathode Material for High Capacity Zinc-Ion Battery

Saad Zafar[a], Muskan Sharma[a], Krithik Shai MP[b], Naiwrit Karmodak[b], Santosh K. Singh[c], Bimlesh Lochab[a]**

[a]Materials Chemistry Laboratory, Department of Chemistry, School of Natural Sciences, Shiv Nadar Institution of Eminence, Gautam Buddha Nagar, Uttar Pradesh 201314, India.

[b]Computational Materials and Electrocatalysis Lab, Department of Chemistry, School of Natural Sciences, Shiv Nadar Institution of Eminence, Gautam Buddha Nagar, Uttar Pradesh 201314, India.

[c]Electrochemical Energy Laboratory, Department of Chemistry, School of Natural Sciences, Shiv Nadar Institution of Eminence, Delhi-NCR-201314, India

Email: santoshk.singh@snu.edu.in; bimlesh.lochab@snu.edu.in

Table of content

Figure S9. Electrochemical performance of VOH for ZIBs. (a) CV curves for the initial four cycles at 0.2 mV s^{-1}; (b) rate capability plot recorded at different current densities; (c) EIS spectra of the pristine and 25th discharged states; and (d) cycling performance at 0.5 A g^{-1}.

Figure S10. Stable binding configurations of zinc ion with the respective amine in V_2O_5.

Figure S11. Schematic illustration of a single step of the GITT during discharge process.

Figure S12. FTIR spectra of VOP2A at initial and discharged states.

Figure S13. Ex situ XPS patterns of the VOP2A sheets at the selected states in the first cycle. (a) wide-survey spectra at pristine, discharged (0.2 V) and charged (1.6 V) state, (b, c) High-resolution XPS spectra of N 1s, and C 1s at various states.

Figure S14. Ex-situ EDS mapping results of VOP2A after discharging, showing elements; (a) V, (b) O, (c) Zn, (d) N and (e) C.

Figure S15. FESEM analysis of the cathode and anode materials of a coin cell at different charge–discharge cycles: (a-d) FESEM images of the VOP2A cathode, and (e-h) FESEM images of the zinc anode.

Materials and Methods

Materials. Vanadium pentoxide (V_2O_5, 98%), PEG-1-Amine, PEG-2-Amine, PEG-3-Amine (Broadpharm, 98%), zinc trifluoromethane sulfonate [Zn-$(CF_3SO_3)_2$], and N-methyl-2-pyrrolidone (NMP), were procured from Sigma Aldrich used without further purification. Grafoil® paper and Celgard®-3501 were procured from Global Nanotech, India.

Synthesis of V_2O_5-PEG-Amine. In a typical synthesis procedure, 0.4 g of V_2O_5 powder and 80 µL of PEG-Amine with variable chain length (PEG-1-Amine, PEG-2-Amine and PEG-3Amine) were dispersed in 30 mL of H_2O under stirring for a homogeneous solution. The solution was then transferred to a 50 mL Teflon-lined stainless-steel autoclave and kept at 180℃ for 10 h in a convection oven. After being naturally cooled to room temperature, the black precipitate was collected and washed with water and ethanol three times. Finally, the product was collected by vacuum filtration and dried in a vacuum oven at 60 °C for 8 h. V_2O_5-PEG-Amine composites containing variable PEG-Amine chain length of PEG-1-Amine, PEG-2-Amine, and PEG-3-Amine are denoted as VOP1A, VOP2A, and VOP3A, respectively. As a control sample V_2O_5 was treated hydrothermally without PEG-Amine which is abbreviated as VOH.

Characterization. The surface morphology and elemental mapping of the copolymer was examined using a field emission scanning electron microscope (FESEM), Jeol JSM-7610Plus coupled with an energy-dispersive X-ray (EDX, AMETEK) detector, under an acceleration voltage of 15 kV. Transmission electron microscopy (TEM) images were recorded using an HRTEM, JEOL-2100F instrument under an accelerating voltage of 200 kV, and d-spacing was calculated using GATAN software. Powder X-ray diffraction (PXRD) was recorded using a Bruker D8 diffractometer, using Cu Kα (λ = 1.5406 Å) in the scattering range (2θ) of 10–80° at room temperature. FTIR spectra were recorded on a Nicolet iS20 spectrometer equipped with an interferometer, KBr/Ge-coated beam splitter, DTGS detector, and attenuated total reflectance diamond (iD5-ATR) accessory. Sixty-four scans at a resolution of 4 cm^{-1} were recorded in the range of 4000–400 cm^{-1}, averaged, and referenced against air. Thermogravimetric analysis (TGA) was recorded with a built-in gas controller (TGA2 SF/1100) and fitted with an XP1U TGA balance (ultra-microbalance) under a 50 mL/min flow rate of nitrogen and zero air in the temperature range of 35–800 °C at a heating rate of 10 °C/min. Raman spectroscopy measurements were carried out with an STR500 Airix microscope using a 532 nm laser at a power of 3 mW. X-ray photoelectron spectroscopy (XPS) measurements were carried out using a Thermo Fisher NEXSA surface analyzer with a monochromatized Al-Kα (1486.7 eV) radiation source to determine the chemical composition and binding energy (BE). The acquired spectrum was charge-corrected at a BE of carbon 1s peak at 284.6 eV and processed with the CasaXPS software. The porosity and surface area were found by Brunauer-Emmer-Teller (BET) (Nova Touch LX2, Quantachromme).

Electrochemical testing. The electrochemical properties of VOPA nanosheets are examined as a cathode material for ZIBs via CR2032-type coin cell assembled in open air under room temperature. The electrodes were prepared via a slurry-casting method. The active materials, conductive additive (Super P), and binder (polyvinylidene fluoride (PVDF)) in a weight ratio of 8:1:1 were mixed in 1-methyl-2-pyrrolidinone (NMP) to prepare the slurry. After being ground uniformly, the electrode slurry was coated onto a Grafoil® foils and dried under vacuum at 60 °C overnight. The active mass loading is 2.9-3.2 mg cm^{-2}. The specific capacity of the electrode was calculated according to the total mass of active materials. A zinc plate, Celgard® (3501) and 3 M Zn $(CF_3SO_3)_2$[1] were used as the anode, separator and aqueous electrolyte, respectively. The cyclic voltammetry (CV) and electrochemical impedance spectroscopy (EIS) were carried out on the electrochemical workstation (BioLogic VMP3). EIS measurement was carried out at open circuit

potentials with a frequency ranging from 200 MHz to 10 Hz. The rate performance was conducted in the voltage range of 0.2-1.6 V (vs. Zn^{2+}/Zn) at different current density. To monitor the electrode capability at higher current rates, the stability was tested at a high current density of 3.0 A g^{-1} for thousands of cycles. The galvanostatic intermittent titration technique (GITT) was applied to analyze the reaction and diffusion kinetics of the cathodes. Before the GITT measurement, the assembled cell was first discharged and charged at 100 mA g^{-1} for 10 cycles to obtain a stable state. Subsequently, the assembled cell was discharged or charged at 50 mA g^{-1} for 20 min, and then relaxed for 1 h to make the voltage reach the equilibrium. The procedure was repeatedly applied to the cell during the entire charge-discharge process until reaching to the cut-off voltage.

For coin cell, the energy density and power density were obtained by the following equations:

$$E = \int_0^{\Delta t} \frac{V \times i}{m} dt \qquad \text{S1}$$

$$P = \frac{E}{1000 \times \Delta t} \qquad \text{S2}$$

where E (Wh kg^{-1}) is the energy density, P is the power density (kW kg^{-1}), V (V), i (mA), m (g) and Δt (h) represent the working potential, discharging current, the mass loading of the cathode and the discharging time, respectively.

Computational details. All the density functional theory (DFT) calculations were conducted by the Vienna ab initio Simulation package (VASP).[2, 3] The electron exchange was incorporated using the Generalized Gradient Approximation (GGA)[4] with Perdew Burke Ernzerhof (PBE) functional. PAW pseudopotentials[5] were employed to treat the electron–ion interactions and the plane wave basis set with energy cutoff 400 eV and (1 × 1 × 1) k point mesh[6] were used for modeling the orbital wavefunctions. The convergence threshold for electronic energy was set to 10^{-6} eV in energy and 10^{-3} eV $Å^{-1}$ for force. The charge density difference plots were obtained using the VESTA[4, 7] package based on the charge density calculations performed using the VASP software. The projected density of states (PDOS) plots was obtained from the calculations from VASP and plotted using wxDragon.[8]

V_2O_5 structure was downloaded from Materials Project Database.[9] PEG amines were oriented in different orientations to see the best binding possibilities. The most distinct orientations were based on their hydrogen bonding abilities. Zinc ions were placed near the PEG amines based

on three main possibilities. All proximities near the amine and oxygen (from amine and V_2O_5 layer) were considered and were averaged to calculate the binding energies.

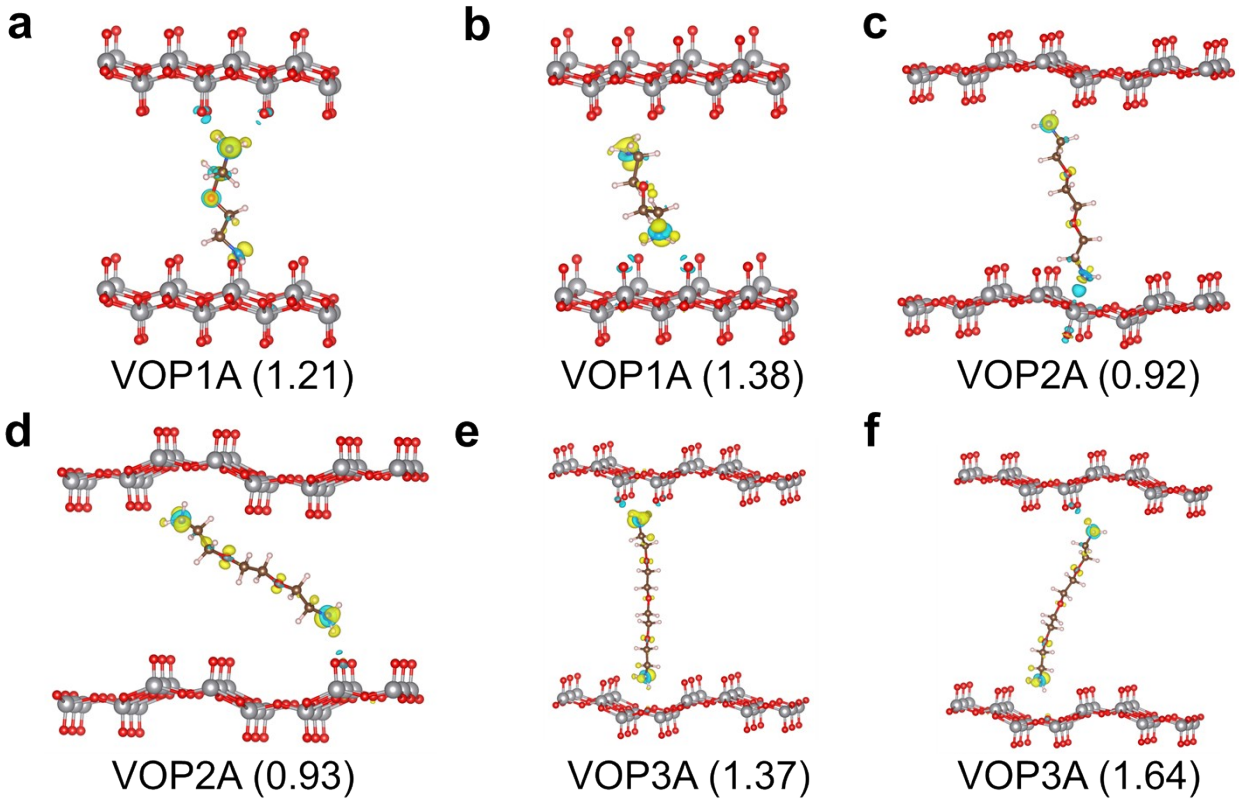

Figure S1. Charge density illustrated optimized geometries of VOP1A, VOP2A and VOP3A in vertical and slant configurations. The relative binding energy (eV) with horizontal orientation as the reference.

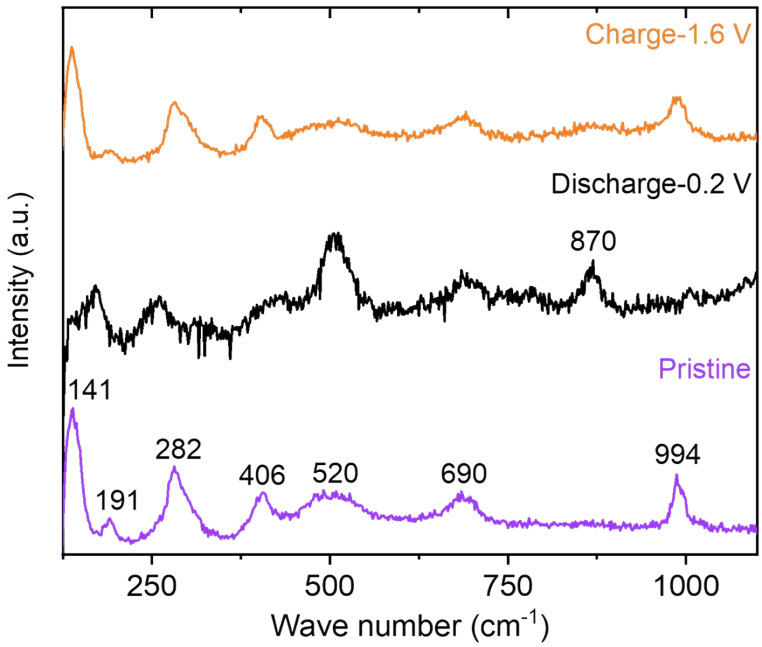

Figure S2. Raman spectrum of VOP2A sample at pristine, discharge (0.2 V) and charged (1.6 V) state.

Peak at 141 and 191 cm^{-1} points towards good crystallinity and corresponds to relative motion of V_2O_5 layers with respect to each other as an outcome of layered structure of V_2O_5. Peaks at 282 and 406 cm^{-1} correspond to bending vibration of V=O while the shoulder peak at 481 cm^{-1} is for bending vibration of V–O–V. The stretching and bending modes of V–O generate peaks at 520 and 690 cm^{-1}. And the shift at 994 cm^{-1} is due to stretching mode of V=O.[10]

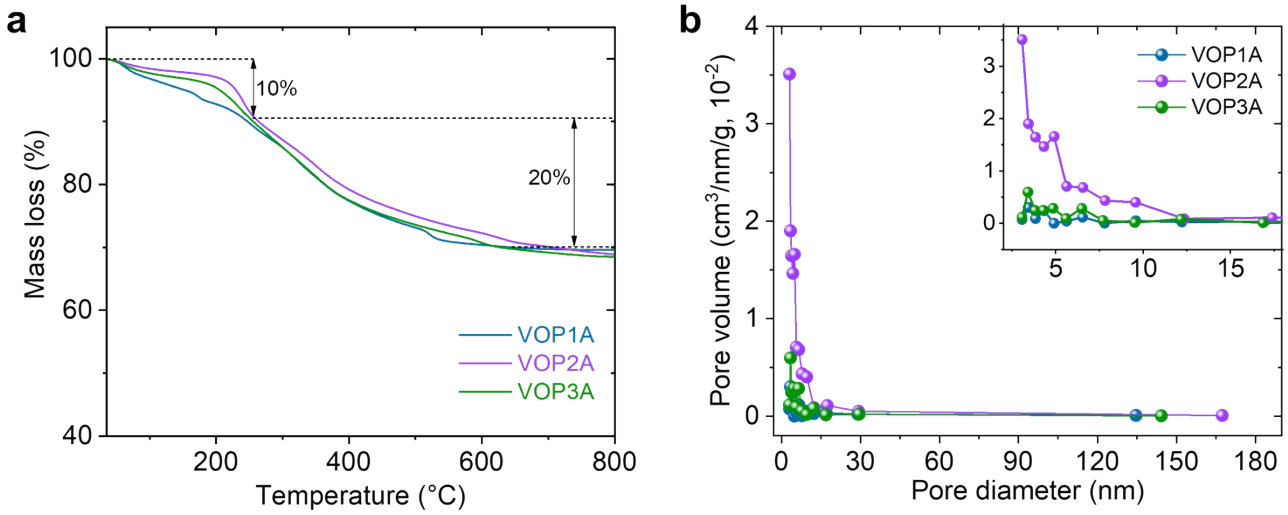

Figure S3. (a) Thermogravimetric analysis (TGA), (b) Pore diameter analysis.

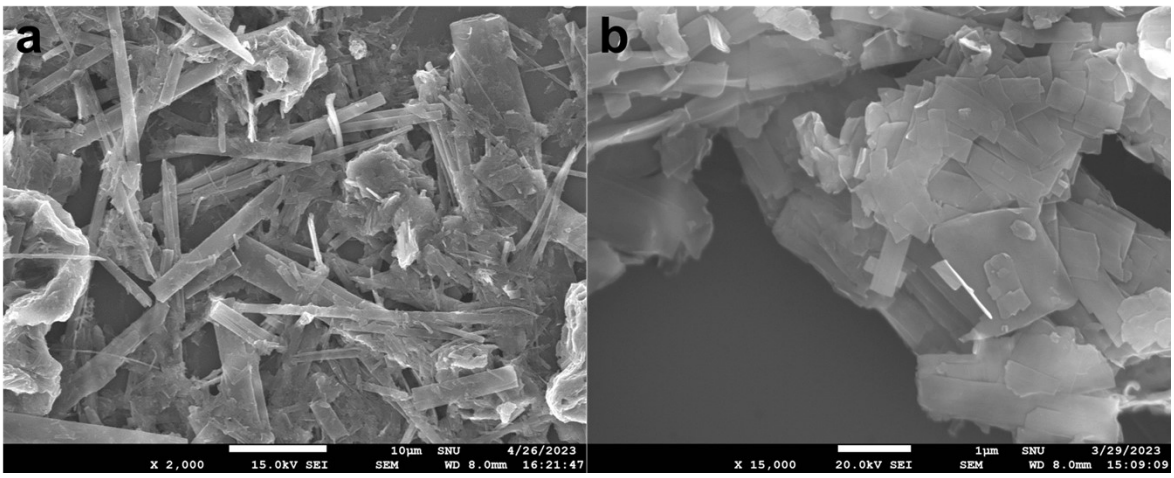

Figure S4. FESEM image of (a) VOP1A nanorods, and (b) VOP3A nanosheets.

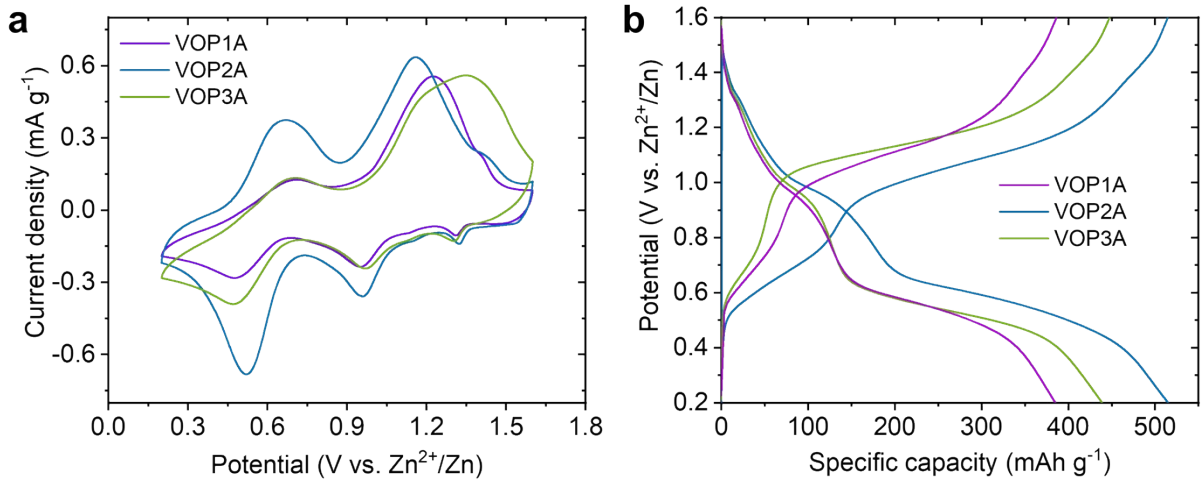

Figure S5. Electrochemical measurements of VOP1A, VOP2A and VOP3A for ZIBs. (a) CV curves at 0.2 mV s^{-1}; and (b) GCD curve of the ZIB at 100 mA g^{-1} current rate.

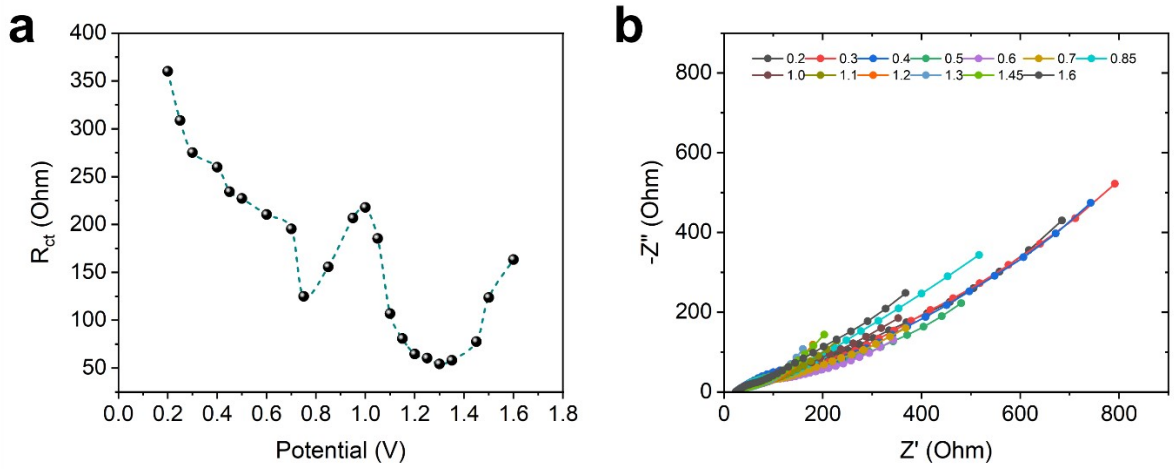

Figure S6. (a) Plot of R_{ct} at different potentials with an interval of 0.05 V from 0.2 V to 1.6 V, and (b) EIS data recorded at different potentials.

The EIS at an interval of 0.05 V from 0.2 V to 1.6 V. From these EIS spectra, we have plotted the Rct value of each plot at different potentials. We have observed a trend in the below presented Figure. When the potential is increased from 0.2 V, the R_{ct} value decreases initially up to 0.75 V and then increases with the increase in the potential till 1.0 V. As the potential increased further the R_{ct} value start to decrease again till 1.3 V and finally reaching to 1.6 V, it has increased again as shown in Figure S6a. Here, if we compare this behaviour with CV data, we can correlate the same pattern in the peaks where redox peak is also observed at 0.66 V and 1.15 V. With the change in the potential during the CV the current value has also changed, the highest current is observed where the Rct value is lowest.

The Warburg region of the Nyquist plot is related with the diffusion of Zn^{2+} in the electrode material. The slope of the Nyquist plot of the Zn//VOP2A battery at low frequencies is shown in Figure S6b, which indicates that the diffusion of Zn^{2+} at the electrode/electrolyte interface of VOP2A is easier (the slope with a linear tendency is smaller, and thus the zinc-ion diffusion in the electrochemical process is faster).

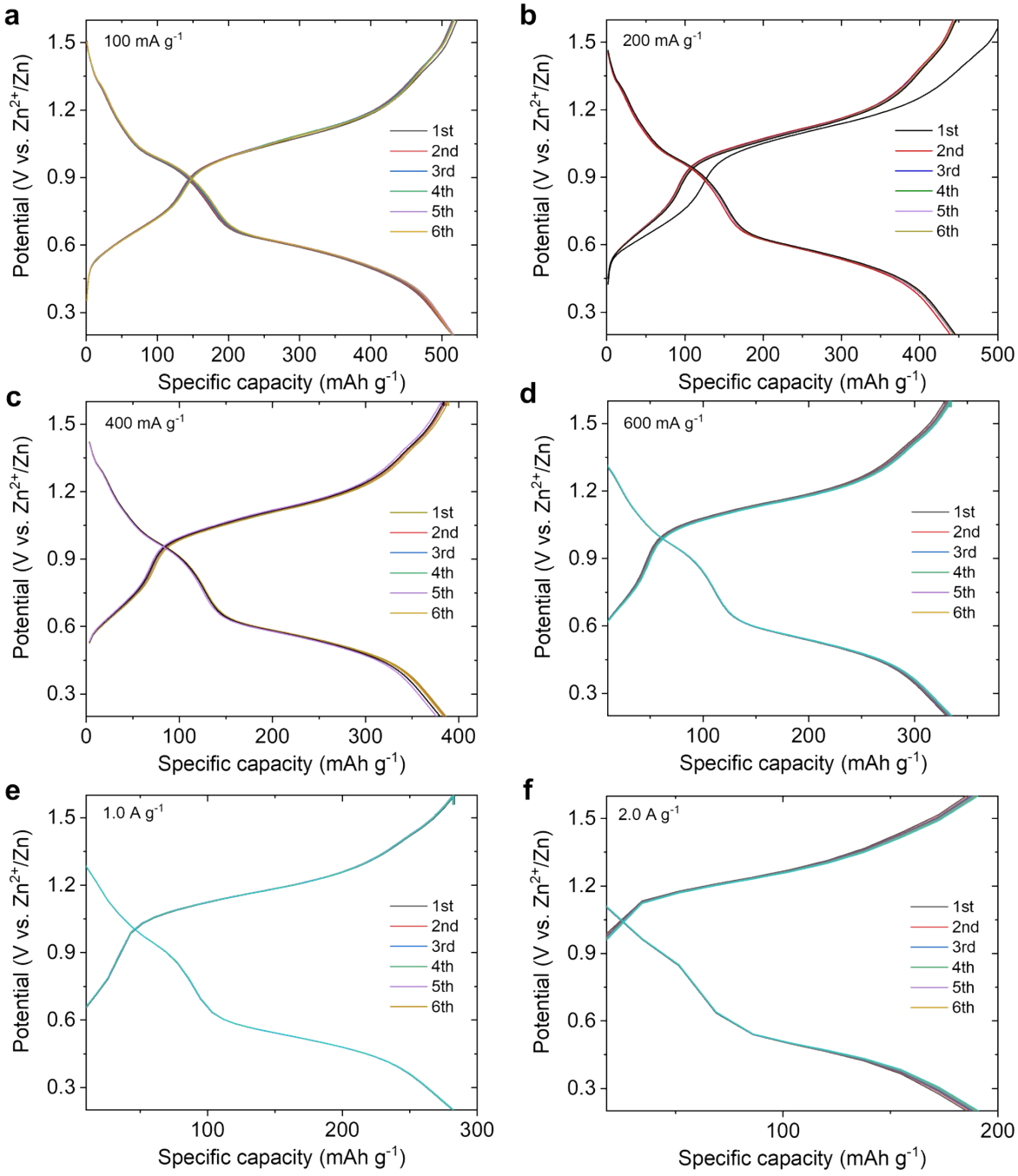

Figure S7. GCD measurements of VOP2A for ZIBs at (a) 100 mA g^{-1}; (a) 200 mA g^{-1}; (a) 400 mA g^{-1}; (a) 600 mA g^{-1}; (a) 1000 mA g^{-1}; and (a) 2000 mA g^{-1}.

Table S1. Comparative performance of vanadium oxide-based cathodes in aqueous zinc-ion battery.

Cathodic Materials	**Electrolyte**	**Capacity (mAh g^{-1}) (Current density) (A g^{-1})**	**Capacity Retention (%) (cycles)**	**Ref.**
VOP2A	**$Zn(CF_3SO_3)_2$**	**515 (0.1)**	**94% (2000)**	**This work**
V_2O_3@C	$Zn(CF_3SO_3)_2$	350 (0.1)	90% (4000)	11
anhydrous V_2O_5	$Zn(CF_3SO_3)_2$	449.8 (0.1)	86.8% (2000)	12
V_2O_5 hollow spheres	$ZnSO_4$	132 (10)	82.5% (6200)	13
V_2O_5	$ZnSO_4$	230.7 (0.2)	87.8% (1000)	14
V_6O_{13}@CC	$ZnSO_4$	227 (9)	99% (1000)	15
PVO	$Zn(OTf)_2$	420 (0.1)	94% (1200)	16
V2O5- YS	$Zn(CF_3SO_3)_2$	410 (0.1)	80% (1000)	17
CO_2-V_6O_{13}	$Zn(CF_3SO_3)_2$	471 (0.1)	80% (4000)	18
VOx nanorods (VONs)	ZnCl2	402 (0.26)	~89% (10,000)	19
$H_2V_3O_8$/Mxene	$Zn(CF_3SO_3)_2$	365 (0.2)	~84% (5600)	20
C@V_2O_5	$Zn(CF_3SO_3)_2$	361(0.5)	71% (2000)	21
Vo-V_2O_5-PEDOT	$Zn(CF_3SO_3)_2$	449 (0.2)	94.3% (6,000)	22
V_3O_7 ·H_2O/rGO nanobelts	$ZnSO_4$	352	79% (1000)	23
V_6O_{13} ·nH_2O	$Zn(CF_3SO_3)_2$	395 (0.1)	87% (1000)	24
VO_2 ·$0.2H_2O$	ZnSO4	423 (0.25)	87% (1,000)	25
$Na_2V_6O_{16}$ ·$3H_2O$ nanorods	ZnSO4	325	80% (1,000)	26
CuV_2O_6	$Zn(CF_3SO_3)_2$	427 (0.1)	~100% (3000)	27
$Na_2V_6O_{16}$ ·$2.14H_2O$	ZnSO4 ·7H2O and Na2SO4	466 (0.1)	90% (2000)	28
$K_{0.5}V_2O_5$	ZnSO4	150 (5)	75% (3000)	29
$Na_{1.25}V_3O_8$	$Zn(CF_3SO_3)_2$	390 (0.1)	88.2% (2000)	30
NaV_6O_{15} microflowers	$Zn(CH_3F_3SO_3)_2$	~300 (0.1)	~107% (2000)	31
$Zn_{0.1}V_2O_5$ ·nH_2O (ZnVO)	ZnSO4	463 (0.2)	88% (20000)	32
NaV_6O_{15}/V_2O	$Zn(CH_3F_3SO_3)_2$	390 (0.3)	92.3% (3000)	33
PEDOT@YVO	$Zn(CF_3SO_3)_2$	308.5 (0.2 C)	79.2% (4000)	34

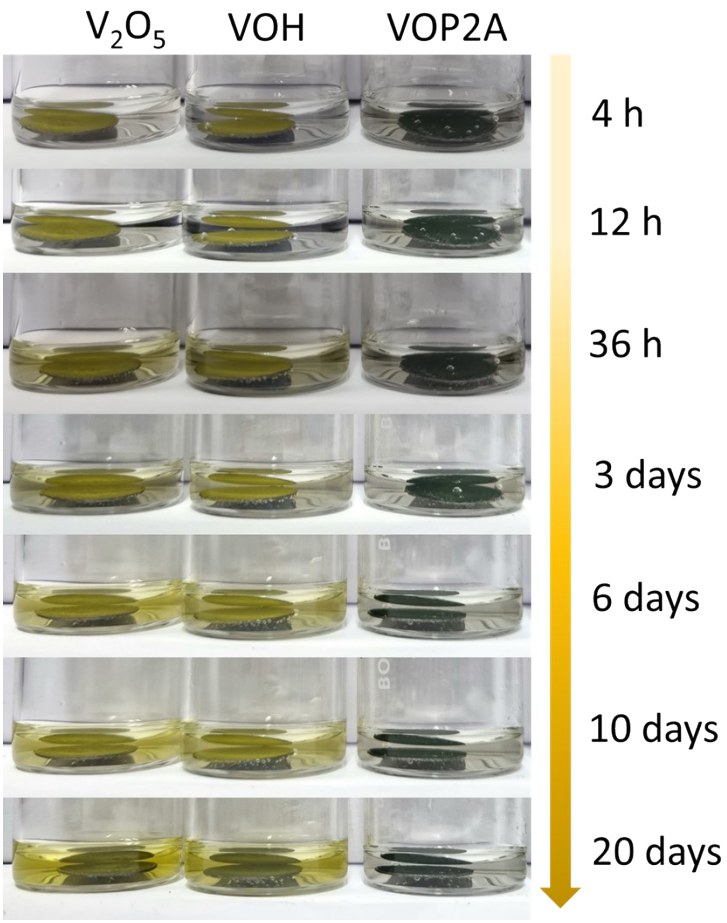

Figure S8. Optical images of electrodes immersed in 3 M $Zn(CF_3SO_3)_2$ aqueous solution with different soaking times.

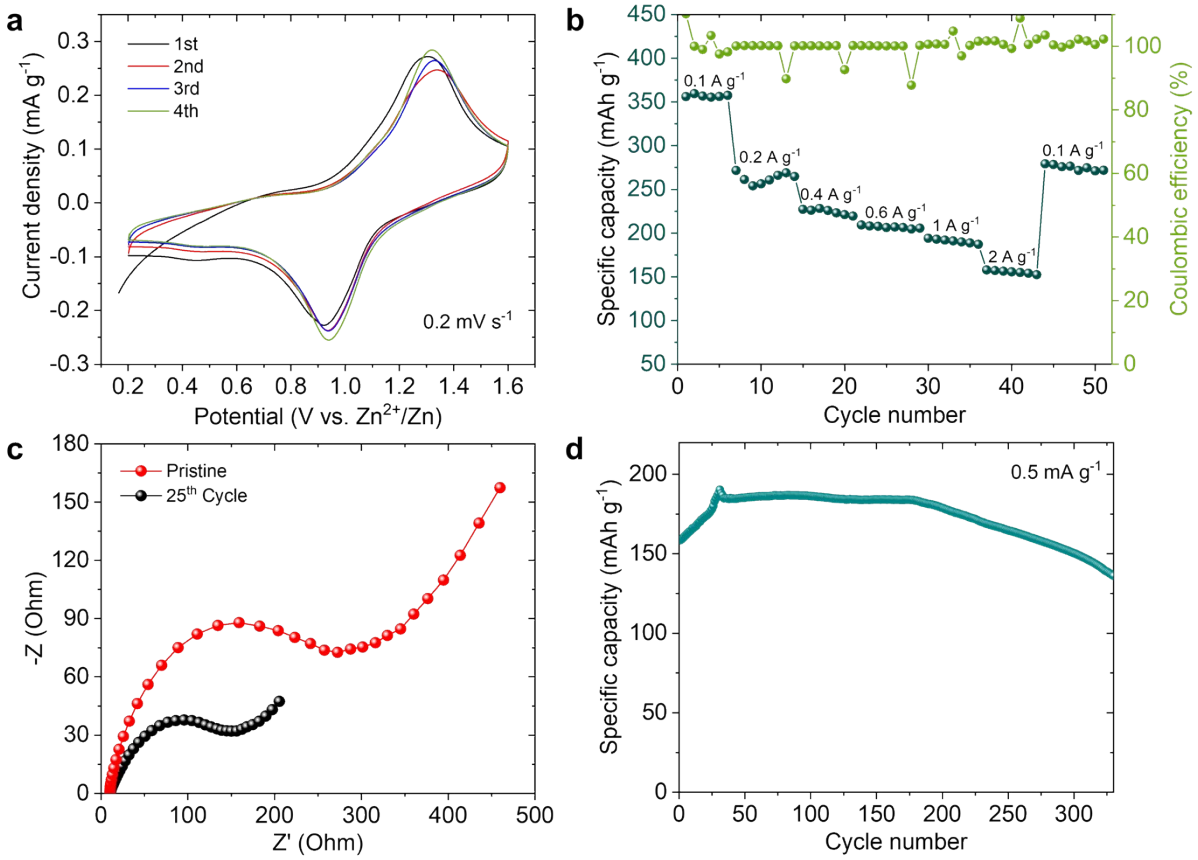

Figure S9. Electrochemical performance of VOH for ZIBs. (a) CV curves for the initial four cycles at 0.2 mV s^{-1}; (b) rate capability plot recorded at different current densities; (c) EIS spectra of the pristine and 25th discharged states; and (d) cycling performance at 0.5 A g^{-1}.

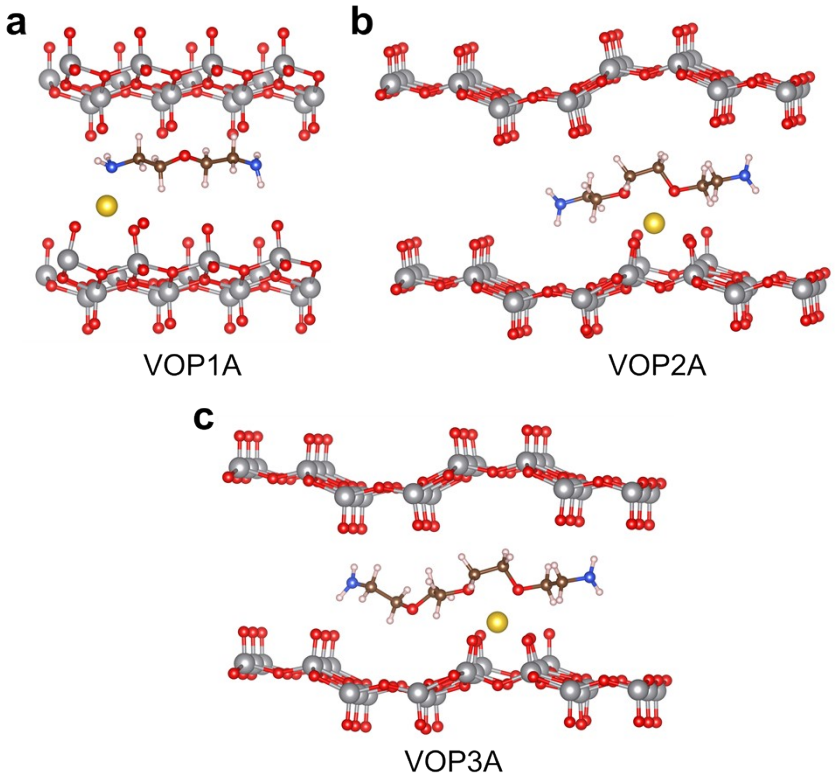

Figure S10. Stable binding configurations of zinc ion with the respective amine in V_2O_5.

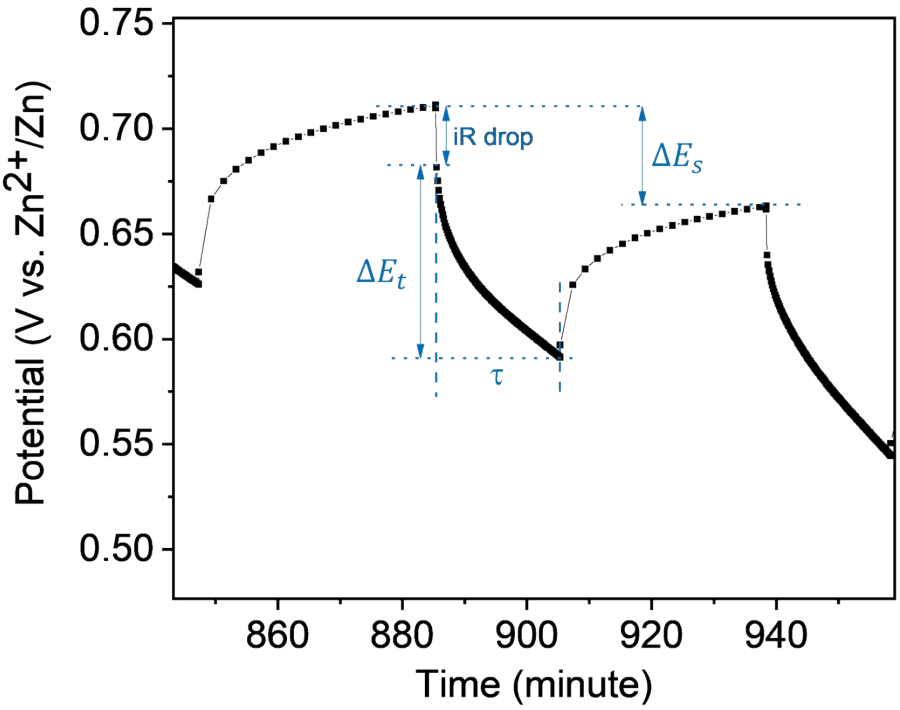

Figure S11. Schematic illustration of a single step of the GITT during discharge process.

From the GITT experiment ion-diffusion coefficient can be calculated using the following equation Eq. S3.

$$D_{Zn^{2+}} = \frac{4}{\pi\tau}\left(\frac{n_m V_m}{S}\right)^2\left(\frac{\Delta E_S}{\Delta E_\tau}\right)^2 \qquad \text{S3}$$

Where, τ is the duration of the current pulse (in seconds); n_m and V_m are the molar mass (mol) and volume (cm^3/mol) of the active material; S is area of the electrode (cm^2); ΔE_S is the steady-state voltage change due to the current pulse and ΔE_τ is the voltage change during the constant current pulse, eliminating the iR drop. The VOP2A cathode is consisted of nanosheet morphology, so by taking 20 nanosheets we have calculated the volume of each nanosheet by using the formula, $V = l_x b_x h$ and taking their average.

Afterthat, the calculated volume of rectangular sheet was equated with the volume of sphere i.e., $V = \frac{4}{3}\pi r^3$ and from here we have calculated the R_s (radius). So, the Eq. S3 may be written as Eq. S4.

$$D_{Zn^{2+}} = \frac{4}{\pi\tau}\left(\frac{R_s}{3}\right)^2\left(\frac{\Delta E_S}{\Delta E_\tau}\right)^2 \quad \text{S4}$$

The GITT profile of the VOP2A cathode during discharge is shown in Figure S11. Each discharge step is composed of 20 minutes of galvanostatic discharge, followed by 60 minutes of relaxation time. The two discharge steps are chosen to estimate the value of ion-diffusion coefficient. The values of ΔE_S and ΔE_τ were estimated to be 5.1 mV and 9.3 mV. Now, we can calculate the diffusion coefficient putting the values of each parameter in Eq. S4.

τ (duration of the current pulse) = 1200 sec,

R_s (radius) = 148.5 nm or 1.48×10^{-5} cm,

ΔE_S (steady-state voltage change due to the current pulse) = 5.1 mV,

ΔE_τ (voltage change during the constant current pulse) = 9.3 mV,

Hence, D = 4.536×10^{-15} cm^2 s^{-1}.

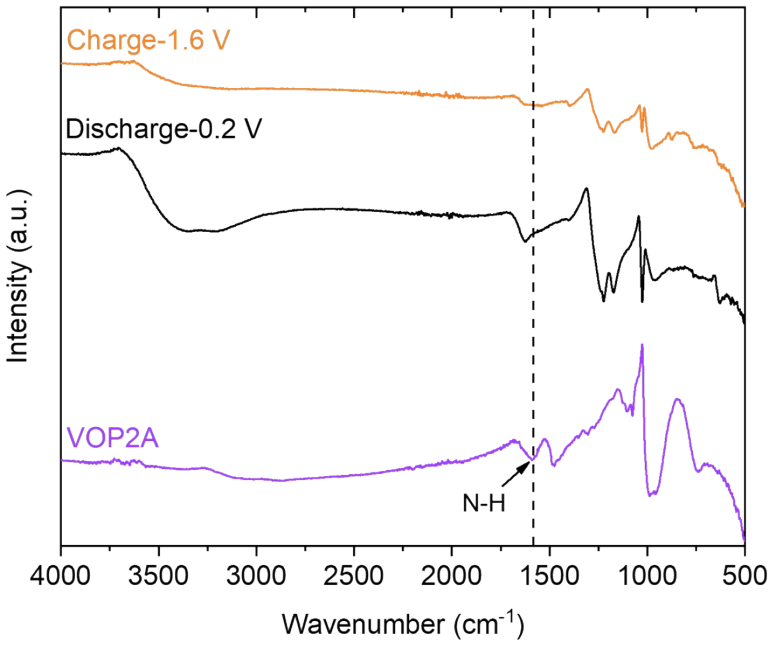

Figure S12. FTIR spectra of VOP2A at initial and discharged states.

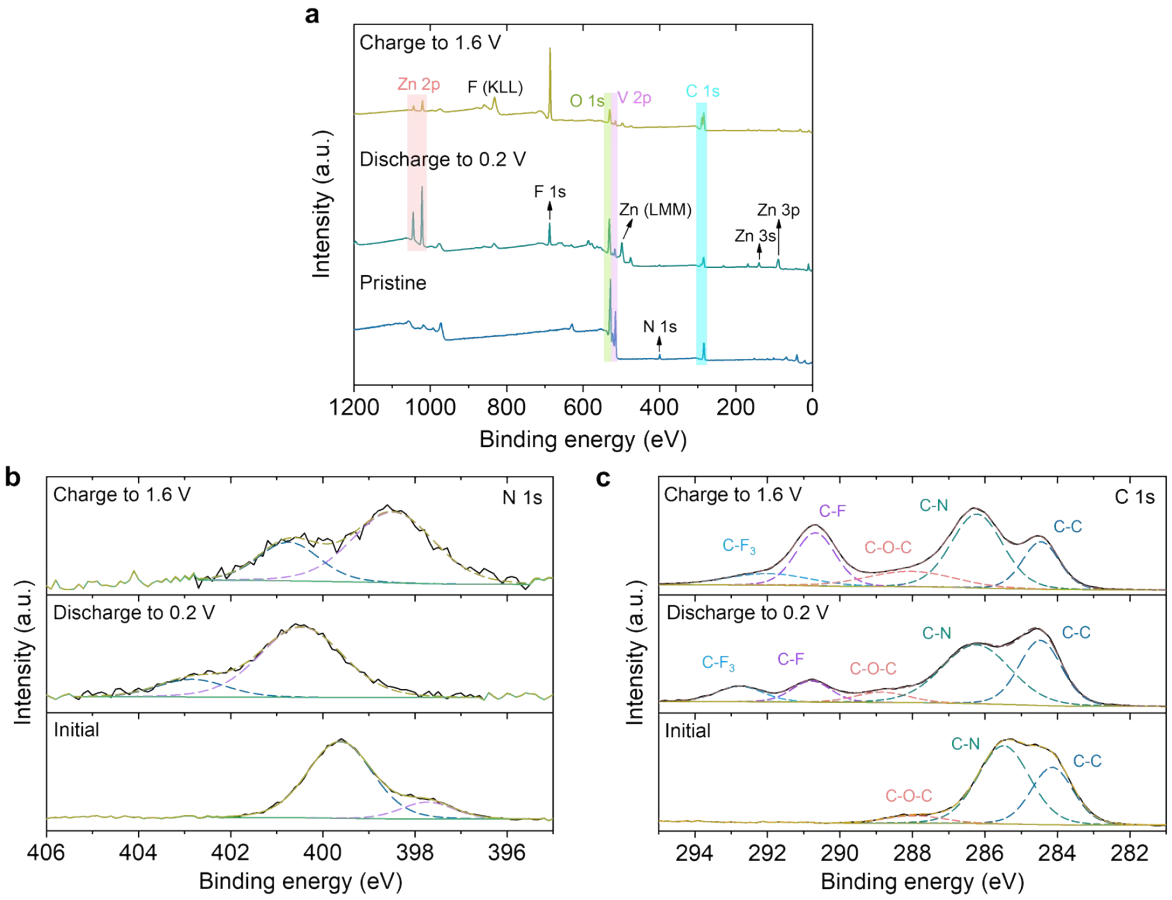

Figure S13. Ex situ XPS patterns of the VOP2A sheets at the selected states in the first cycle. (a) wide-survey spectra at pristine, discharged (0.2 V) and charged (1.6 V) state, (b, c) High-resolution XPS spectra of N 1s, and C 1s at various states.

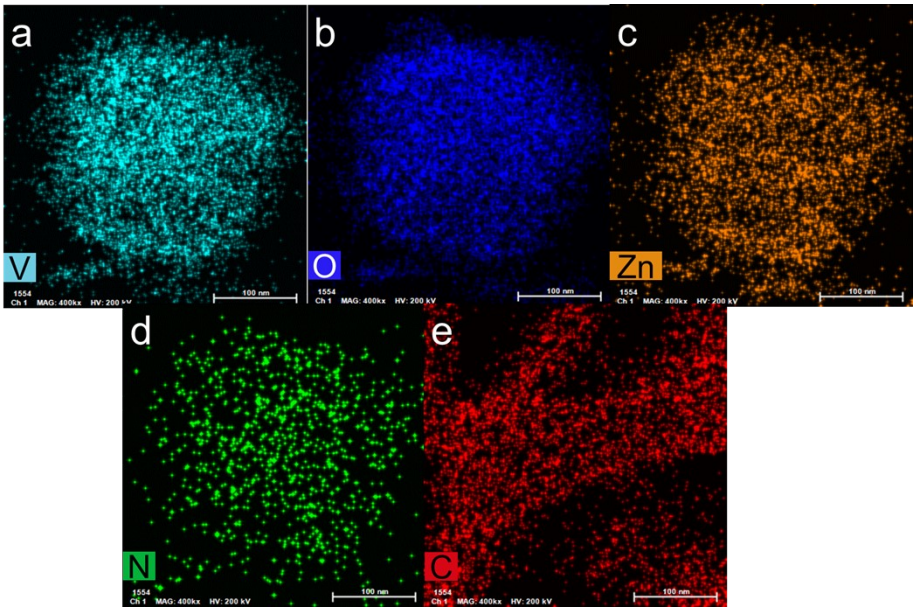

Figure S14. Ex-situ EDS mapping results of VOP2A after discharging, showing elements; (a) V, (b) O, (c) Zn, (d) N and (e) C.

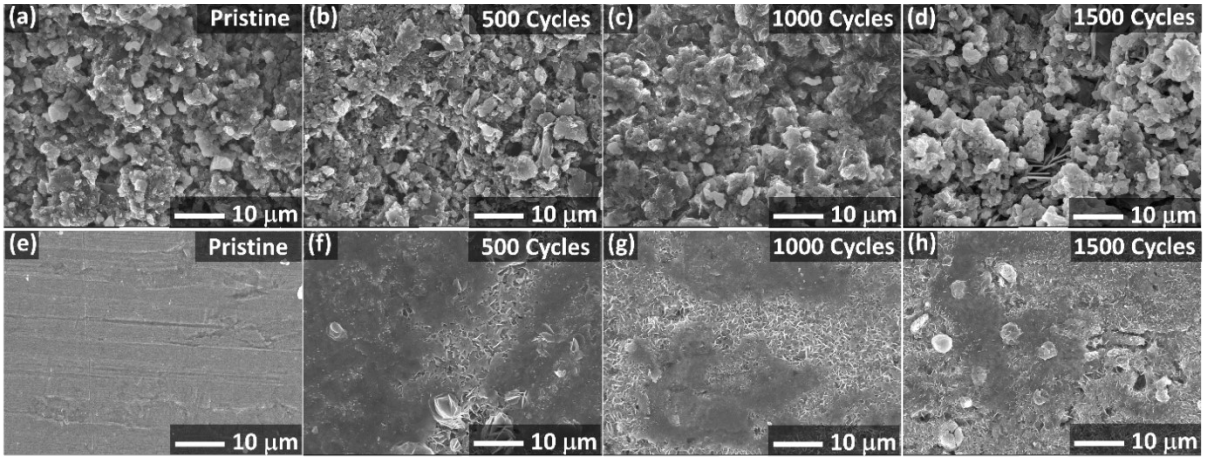

Figure S15. FESEM analysis of the anode and cathode materials of a coin cell at different charge–discharge cycles: (a-d) VOP2A cathode, and (e-h) zinc anode.

Reference:

1. N. Zhang, F. Cheng, Y. Liu, Q. Zhao, K. Lei, C. Chen, X. Liu and J. Chen, *J. Am. Chem. Soc.*, 2016, **138**, 12894-12901.
2. G. Kresse and J. Hafner, *Phys. Rev. B. Condens. Matter*, 1993, **48**, 13115.
3. G. Kresse and J. Furthmüller, *Comput. Mater. Sci.*, 1996, **6**, 15-50.
4. J. P. Perdew, K. Burke and M. Ernzerhof, *Phys. Rev. Lett.*, 1996, **77**, 3865.
5. G. Kresse and D. Joubert, *Phys. Rev. B*, 1999, **59**, 1758.
6. H. J. Monkhorst and J. D. Pack, *Phys. Rev. B*, 1976, **13**, 5188-5192.
7. K. Momma and F. Izumi, *J. Appl. Cryst.*, 2008, **41**, 653-658.
8. S. Maintz, V. L. Deringer, A. L. Tchougréeff and R. Dronskowski, *J. Comput. Chem.*, 2013, **34**, 2557-2567.
9. A. Jain, S. P. Ong, G. Hautier, W. Chen, W. D. Richards, S. Dacek, S. Cholia, D. Gunter, D. Skinner, G. Ceder and K. A. Persson, *APL Mater.*, 2013, **1**.
10. D. Surya Bhaskaram, R. Cheruku and G. Govindaraj, *J Mater Sci: Mater Electron*, 2016, **27**, 10855-10863.
11. Y. Ding, Y. Peng, S. Chen, X. Zhang, Z. Li, L. Zhu, L.-E. Mo and L. Hu, *ACS Appl. Mater. Interfaces*, 2019, **11**, 44109-44117.
12. W. Zhou, J. Chen, M. Chen, X. Xu, Q. Tian, J. Xu and C.-P. Wong, *RSC Adv.*, 2019, **9**, 30556-30564.
13. H. Qin, L. Chen, L. Wang, X. Chen and Z. Yang, *Electrochim. Acta*, 2019, **306**, 307-316.
14. Y. Chen, K. Xiang, Y. Zhu, L. Xiao, W. Chen, H. Liao, X. Chen and H. Chen, *J. Electrochem. Soc.*, 2019, **166**, A2805.
15. M. Tamilselvan, T. V. M. Sreekanth, K. Yoo and J. Kim, *Appl. Surf. Sci.*, 2020, **529**, 147077.
16. R. Li, H. Zhang, J. Yan, Q. Zheng and X. Li, *Fundam. Res.*, 2021, **1**, 425-431.
17. R. Li, H. Zhang, Q. Zheng and X. Li, *J. Mater. Chem. A*, 2020, **8**, 5186-5193.
18. W. Shi, B. Yin, Y. Yang, M. B. Sullivan, J. Wang, Y.-W. Zhang, Z. G. Yu, W. S. V. Lee and J. Xue, *ACS Nano*, 2021, **15**, 1273-1281.
19. Q. Pan, R. Dong, H. Lv, X. Sun, Y. Song and X.-X. Liu, *Chem. Eng. J.*, 2021, **419**, 129491.
20. C. Liu, W. Xu, C. Mei, M.-C. Li, X. Xu and Q. Wu, *Chem. Eng. J.* , 2021, **405**, 126737.
21. C. Liu, R. Li, W. Liu, G. Shen and D. Chen, *ACS Appl. Mater. Interfaces*, 2021, **13**, 37194-37200.
22. Y. Du, X. Wang and J. Sun, *Nano Res.*, 2021, **14**, 754-761.
23. C. Shen, X. Li, N. Li, K. Xie, J.-g. Wang, X. Liu and B. Wei, *ACS Appl. Mater. Interfaces*, 2018, **10**, 25446-25453.
24. J. Lai, H. Zhu, X. Zhu, H. Koritala and Y. Wang, *ACS Appl. Energy Mater.*, 2019, **2**, 1988-1996.
25. D. Jia, K. Zheng, M. Song, H. Tan, A. Zhang, L. Wang, L. Yue, D. Li, C. Li and J. Liu, *Nano Res.*, 2020, **13**, 215-224.
26. V. Soundharrajan, B. Sambandam, S. Kim, M. H. Alfaruqi, D. Y. Putro, J. Jo, S. Kim, V. Mathew, Y.-K. Sun and J. Kim, *Nano Lett.*, 2018, **18**, 2402-2410.
27. Y. Liu, Q. Li, K. Ma, G. Yang and C. Wang, *ACS Nano*, 2019, **13**, 12081-12089.
28. F. Hu, D. Xie, D. Zhao, G. Song and K. Zhu, *J. Energy Chem.*, 2019, **38**, 185-191.
29. Y. Hao, S. Zhang, P. Tao, T. Shen, Z. Huang, J. Yan and Y. Chen, *ChemNanoMat*, 2020, **6**, 797-805.
30. D. Xie, F. Hu, X. Yu, F. Cui, G. Song and K. Zhu, *Chin. Chem. Lett.*, 2020, **31**, 2268-2274.
31. R. Li, C. Guan, X. Bian, X. Yu and F. Hu, *RSC Adv.*, 2020, **10**, 6807-6813.
32. K. Zhu, T. Wu, W. van den Bergh, M. Stefik and K. Huang, *ACS Nano*, 2021, **15**, 10678-10688.
33. L. Fan, Z. Li, W. Kang and B. Cheng, *J. Energy Chem.*, 2021, **55**, 25-33.
34. J. Kumankuma-Sarpong, W. Guo and Y. Fu, *Small Methods*, 2021, **5**, 2100544.